The interplay between small RNA pathways shapes chromatin landscape in *C. elegans*

E. Gushchanskaia[1], R. Esse[1], Q. Ma[1], N. Lau[1], A. Grishok[1*]

[1]Boston University School of Medicine, Biochemistry Department, Boston, 02118, USA

The nematode *C. elegans* contains numerous endogenous small RNAs produced by RNA-dependent RNA polymerase complexes. The DRH-3 helicase, a component of RdRP, is required for production of both “silencing” siRNAs bound by Worm-specific Argonautes (WAGO) and “activating” siRNAs bound by CSR-1. Here we show that in the *drh-3(ne4253)* mutant deficient in the RdRP-produced secondary endo-siRNAs there is an ectopic accumulation of H3K27me2 at highly expressed genes. Moreover, we observe ectopic H3K9me3 at the enhancer elements in both *drh-3(ne4253)* and *csr-1(tm892)* mutant backgrounds. Notably, our previous work described a global increase in antisense transcription upon *csr-1* and *drh-3* loss-of function, and now we also report an increase in enhancer RNA levels in these mutants. We propose that, in the absence of secondary siRNAs, elevated antisense transcription promotes nuclear dsRNA formation, which, in turn, can be cleaved by Dicer into primary siRNAs that guide deposition of silent chromatin marks. A change in the siRNA landscape in RdRP and *drh-3(ne4253)* mutants and accumulation of dsRNA in the nuclei of *drh-3(ne4253)* worms supports this model.

INTRODUCTION

Research in fission yeast and plants identified an elaborate connection between small RNAs and heterochromatin formation (Reinhart et al., 2002; Pikaard and Mittelsten Scheid, 2014). To what extent this mechanism is conserved in other species is an important biological question. Exogenous or transgene-based introduction of the double-stranded RNA (dsRNA) was shown to initiate transcriptional silencing and/or heterochromatin formation in *C. elegans* (Grishok et al., 2005; Gu et al., 2012; Burton et al., 2011) and mammalian cells (Gullerova and Proudfoot, 2012). With the discovery of a new class of small RNAs, piRNAs, and their role in protecting germline from parasitic elements, the connection between small RNAs and chromatin in animals has been increasingly attributed to piRNAs (Cecere and Grishok, 2014). Although endogenous siRNAs (endo-siRNAs) produced from the dsRNA segments arising from large hairpins, overlapping 5' or 3' ends of transcripts, or repetitive elements have been detected in oocytes of higher animals (Watanabe et al., 2008; Tam et al., 2008), their biological significance remains unclear. Most recently, the possibility of nuclear small RNA production at the enhancers (Li et al., 2016) brought renewed interest in the regulatory potential of nuclear RNAi in animals.

In *C. elegans*, primary siRNAs generated through long dsRNA cleavage by the Dicer complex have been described in silencing induced by exogenous dsRNA (Yigit et al., 2006) or during viral infection (Sarkies et al., 2013). Consistently, the long dsRNA-binding protein RDE-4 (Tabara et al., 2002) and

the primary siRNA-binding Argonaute RDE-1 (Yigit et al., 2006), which are required for these processes, are often referred to as antiviral RNAi pathway components. However, in the absence of *C. elegans* ADARs, there is ectopic accumulation of nuclear dsRNA substrates for Dicer and ectopic activation of the antiviral RNAi pathway, which leads to developmental and physiological abnormalities (Warf et al., 2012). Most recently, Bass and colleagues described novel abundant endogenous primary siRNAs accumulating in the ADAR mutants that are likely responsible for these negative effects (Reich et al., 2018).

In wild type worms, the most abundant endo-siRNAs are 22G-RNAs produced by RNA-dependent RNA Polymerases (RdRP). In the antiviral pathway, primary siRNAs bound by RDE-1 are ultimately responsible for the recruitment of RdRPs to the 3' uridylated mRNA fragments and amplification of the RNAi response through secondary 22G-RNAs (Tsai et al., 2015). In the endogenous RNAi pathways, either ERGO-1-bound primary siRNAs or piRNAs initiate 22G-RNA production (Yigit et al., 2006; Han et al., 2009; Vasale et al., 2010; Ashe et al., 2012; Buckley et al., 2012; Gu et al., 2012b; Luteijn et al., 2012; Shirayama et al., 2012)). These pathways target repetitive elements, pseudogenes, transposons and some duplicated protein-coding genes for silencing. A group of redundant Worm-specific AGO proteins (WAGO) bind 22G-RNAs generated downstream of both antiviral and endogenous RNAi silencing pathways. The nuclear WAGO implicated in inducing transcriptional silencing are NRDE-3, expressed in the soma, and HRDE-1, expressed in the germline. There is evidence that these proteins are capable of inducing H3K9me3 at

endogenous genes complementary to exogenous dsRNA or at the transgenes, downstream of the piRNAs (Guang et al., 2008; Guang et al., 2010; Burton et al., 2011; Ashe et al., 2012; Buckley et al., 2012; Gu et al., 2012b; Luteijn et al., 2012; Shirayama et al., 2012). At the endogenous WAGO targets, i.e. repetitive elements, pseudogenes, and transposons, the connection between 22G-RNA production, H3K9 methylation and transcriptional silencing is less robust (Moazed et al., 2006; Burkhart et al., 2011; Ni et al., 2014), and the possibility of H3K27 methylation guided by 22G-RNAs has not been widely explored.

CSR-1 (Chromosome Segregation and RNAi deficient) Argonaute (Yigit et al., 2006; Claycomb et al., 2009) is present both in the cytoplasm and the nucleus. It binds 22G-RNAs that are largely antisense to highly and widely expressed genes, and is associated with the nascent transcripts and mature mRNAs complementary to these siRNAs. Elucidating the molecular function of CSR-1 in the nucleus remains challenging, despite the efforts of multiple research groups attracted to this enigmatic Argonaute. The current agreement is that CSR-1 is an “activating” or “anti-silencing” Argonaute, since the levels of nascent transcripts complimentary to CSR-1-bound siRNAs decrease in *csr-1*-deficient worms. However, the mechanism behind this apparent positive role of CSR-1 in gene regulation is not known. Earlier, we took a genomic approach in studying CSR-1 function (Global Ran-on Sequencing or GRO-seq) and detected both a decrease in nascent mRNA transcripts targeted by CSR-1 siRNAs and a remarkable increase in antisense transcription genome-wide in *csr-1* and *drh-3* loss-of-function mutants (Cecere et al., 2014). Notably, DRH-3 (Dicer-related

helicase) is a component of RdRP complexes producing 22G-RNAs and is required for generation of both WAGO-bound and CSR-1 bound small RNAs.

Here, we report a re-distribution of H3K27 methylation from the repetitive elements and X chromosome to active genes (CSR-1 targets) in the *drh-3(ne4253)* mutant worms, which correlates with an increase in antisense transcription at these loci. Moreover, we show that in both *csr-1(tm892)* and *drh-3(ne4253)* there is an increase in enhancer RNA transcription and elevation in H3K9me3 at the enhancers. Finally, we determined that small RNAs remaining on the absence of RdRP function are matching both sense and antisense strands of CSR-1 target pre-mRNAs. Our results support a model that "activating" and "silencing" secondary siRNAs in *C. elegans* have complementary functions required for proper genome-wide chromatin organization. We propose that in the absence of secondary siRNAs, there is excessive dsRNA production and activation of the antiviral RNAi pathway, which has the potential in guiding both H3K9 and H3K27 methylation.

RESULTS

Histone H3K27 methylation is ectopically increased on highly active genes upon *drh-3* loss-of-function

In the earlier studies, we observed similar alterations in global transcription in the viable partial loss-of-function *csr-1(tm892)* and *drh-3(ne4253)* mutant larvae (Cecere et al., 2014). To establish a connection between the transcription changes and chromatin status in these mutants, we performed

ChIP-seq with the antibodies specific to several histone modifications: H3K27me3, H3K36me3, and H3K9me3.

The data obtained using wild type worms were consistent with the previous studies (Schmitges et al., 2011; Yuan et al., 2011; Gaydos et al., 2014) and demonstrated that H3K36me3 was linked to actively transcribed genes, while H3K27me3 was enriched in the regions with low transcription activity (Figure 1A).

In the *drh-3(ne4253)* mutant, transcription reduction of normally highly expressed genes strongly correlated with a reduction in the levels of active histone modification H3K36me3 and a gain of repressive histone mark H3K27me3 (Figure 1B). The highly expressed messages are known to be complementary to CSR-1-bound small RNA (i.e. represent CSR-1 target genes) (Claycomb et al., 2009), and a global reduction in H3K36me3 accompanied by a gain in H3K27me3 occurred at these CSR-1 target genes in *drh-3(ne4253)* (Figure 1C, left panel and Figure 1D).

At the same time, we observed that transcriptionally silent regions (pseudogenes and tissue-specific genes) that become more active in *drh-3(ne4253)* gained H3K36me3 and lost H3K27me3 in the *drh-3(ne4253)* mutant (Supplementary figure 1).

Surprisingly, in the *csr-1(tm892)* mutant, we did not observe dramatic changes in chromatin modifications (Figure 1C, right panel), even though transcription changes similar to those occurring in *drh-3(ne4253)* take place in this mutant as well (Cecere et al., 2014). It is possible that a loss of CSR-1-

interacting siRNAs in *drh-3(ne4253)* causes a more severe effect on the CSR-1/siRNA complex function than a decrease in CSR-1 protein level in the partially rescued *csr-1(tm892)* mutant (Cecere et al., 2014). Alternatively, the distinct molecular phenotypes, that is: the partial loss of only the "activating" pathway in the *csr-1(tm892)* mutant and the perturbation of both "activating" and silencing pathways in the *drh-3(ne4253)* mutant can result in different changes in chromatin.

Overall, our results indicate that a loss of both "activating" and "silencing" siRNAs results in dramatic redistribution of H3K36me3 and H3K27me3 histone modifications along the gene bodies. We conclude that ectopic H3K27me3 observed at the CSR-1 target genes in *drh-3(ne4253)* cannot be guided by the WAGO pathway, which is not active in this mutant, and there must be additional mechanisms responsible for the deposition of this mark.

Opposite regulation of H3K9me3 on highly active genes by the CSR-1 and WAGO pathways

Another histone modification, H3K9me3, which is associated with heterochromatin and had been connected to the WAGO pathway in several publications (Guang et al., 2008; Guang et al., 2010; Burton et al., 2011; Ashe et al., 2012; Buckley et al., 2012; Gu et al., 2012b; Luteijn et al., 2012; Shirayama et al., 2012), has been analyzed in our study. We found this modification to be predominantly located on the chromosome arms (Figure 2A), consistent with the published data (Liu et al., 2011). Whereas the level of H3K9me3 increased at the

CSR-1 target genes in the *csr-1(tm892)* mutant compared to wild type (Figure 2B, left plot), in *drh-3(ne4253)* we observed a depletion in this silencing mark at the same set of genes (Figure 2B, right plot). Because both the CSR-1 and the WAGO pathways are inhibited by the *drh-3(ne4253)* mutation, these results suggest a competition between the activating and silencing secondary siRNAs, such that the WAGO pathway promotes H3K9me3 and CSR-1 inhibits its deposition at the majority of CSR-1 target genes. This type of competitive relationship has been suggested by numerous studies utilizing transgenic strains (Ashe et al., 2012; Lee et al., 2012; Shirayama et al., 2012).

Our results are consistent with the idea that ectopic H3K27me3 is associated with a reduction in expression of highly active genes in *drh-3(ne4253)*, whereas in *csr-1*(*tm892)* WAGO-induced H3K9me3 is likely to play a more prominent role in inhibiting active genes. Therefore, CSR-1-bound siRNAs must protect highly expressed genes from both WAGO-dependent H3K9me3 deposition and H3K27me3 deposition driven by additional mechanisms.

H3K9me3 increases at enhancer regions in *csr-1(tm892)* and *drh-3(ne4253)* mutants

Notably, we identified a small group of CSR-1 target genes (2.5%) that harbor enhancer elements in their introns (Supplementary figure 2A). In this group, H3K9me3 levels increased in the *drh-3(ne4253)* mutant background (Supplementary figure 2B), similarly to the overall increase observed in *csr-1(tm892)*. Since enhancer-containing genes represent a small group of CSR-1

targets, this observation did not reach statistical significance. However, this initial finding prompted us to investigate H3K9me3 levels specifically at the enhancers. Indeed, in both *csr-1(tm892)* and *drh-3(ne4253)* mutants H3K9me3 was increased at the enhancer regions defined by a recent ATAC-seq study (Daugherty et al., 2017a) (Figure 2C).

From these results we conclude that RdRP-produced small RNAs may promote enhancer function by antagonizing, directly or indirectly, chromatin compaction at these regions.

Increase in antisense RNA production in *csr-1(tm892)* and *drh-3(ne4253)* correlates with silencing marks accumulation

Previously, we described a global increase in antisense transcription in the *csr-1(tm892)* and *drh-3(ne4253)* mutants (Cecere et al., 2014). To determine whether regions showing ectopic silencing marks in these mutants produce antisense RNA, we re-analyzed our published GRO-seq data. Indeed, we detected an increase in antisense transcription at CSR-1 target genes in both mutants, and especially at the genes containing intronic enhancers (Figure 3).

To further analyze transcription associated with the potential enhancer regions, we used enhancer-mapping data from two recent publications (Evans et al., 2016; Daugherty et al., 2017). One of these studies used the established chromatin signature of the enhancers to predict their location (Evans et al., 2016), and another used ATAC-seq to map open chromatin regions associated with the enhancers (Daugherty et al., 2017). The latter one also confirmed the

functionality of some of the enhancers. The first study contained a data set obtained from larval stage 3 (L3), the same developmental stage used in our GRO-seq (Cecere et al., 2014) and ChIP-seq experiments. Our analysis of GRO-seq data identified a global increase in transcription at the putative enhancers in both *csr-1(tm892)* and *drh-3(ne4253)* mutants (Figure 4A). We confirmed this result using the ATAC-seq-based enhancer mapping data set for our analyses, which allowed us to distinguish between the intragenic and intergenic (distal) enhancers (Figure 4B). We found that transcription was increased only at the distal enhancers in the *csr-1(tm892)* mutant, whereas in *drh-3(ne4253)* an increase was observed at both intragenic and distal enhancers, although it was more pronounced at the distal ones (Figure 4B and C).

In summary, we observed an increase in antisense transcription at the CSR-1 target genes and an increase in enhancer RNA transcription (in both directions) in the absence of RdRP-produced small RNAs. These results suggest that double-stranded RNA may accumulate at these regions in the studied mutants and that it may initiate the antiviral RNAi pathway ultimately guiding the deposition of silencing chromatin marks.

dsRNA-derived primary small RNA may induce histone modifications in the absence of secondary siRNAs

To test the idea of dsRNA accumulation in our mutants, we performed immunostaining of the intestinal cells with the antibody recognizing long dsRNA (J2, a generous gift from Dr. Mühlberger). In the *csr-1(tm892)* mutant the

accumulation was not extensive, but in *drh-3(ne4253)* we observed a strong staining signal in the nucleus (Figure 5C). We confirmed the specificity of the antibody by using RNase A-treated control samples (Supplementary figure 3).

Small antisense RNAs are very abundant in the wild type worms, and they are mostly represented by secondary siRNAs produced by RdRPs: 22G RNAs. Therefore, secondary siRNAs should be significantly depleted in the RdRP complex mutants. Two *C. elegans* RdRPs: EGO-1 and RRF-1 have partially overlapping functions in secondary siRNA generation (Gu et al., 2009). The datasets of small RNAs cloned from the RdRP and other mutants are available (Gu et al., 2009; Claycomb et al., 2009). Using these data, we tested the idea that, in the absence of secondary, and mostly antisense, siRNAs produced by RdRP, primary siRNAs produced by the Dicer cleavage may take their place. To accomplish this, we compared the proportion of small antisense RNAs in the wild type and the RdRP complex mutants: *drh-3(ne4253), ego-1(om97),* and *ego-1; rrf-1* (Gu et al., 2009). As expected, antisense RNAs comprised 90-95% of the total pool in wild type. In the RdRP mutants the proportion of antisense RNAs dropped to 50-35% (Figure 5A), consistent with the equal representation of sense and antisense RNAs in the siRNA duplex generated by Dicer.

To specifically examine the changes in the siRNA landscape at the CSR-1 target genes, we chose a cluster of histone genes on chromosome four (Figure 5B). In wild type worms, small RNAs mapping to this region largely correspond to antisense 22G RNAs binding to CSR-1 (Figure 5B, CSR-1 IP track). Strikingly, in the *drh-3(ne4253)* worms, there are more sense than antisense RNAs at this

254 locus, and in the RdRP mutants the symmetric signature of both sense and
255 antisense small RNAs matching each gene becomes apparent.

256 Thus, the nuclear accumulation of dsRNA in *drh-3(ne4253)* and the
257 appearance of the primary siRNA signature in the population of small RNAs
258 present in RdRP mutants strongly suggest that the antiviral RNAi pathway is
259 ectopically activated in the absence of secondary small RNAs.

260 Moreover, the ectopic H3K27me3 at the CSR-1 target genes and
261 H3K9me3 at the enhancers observed in *drh-3(ne4253)* is likely guided by this
262 new population of Dicer-dependent small RNAs. We believe that CSR-1-bound
263 antisense RNAs protect their RNA targets both from the WAGO-induced and
264 antiviral RNAi pathway-induced silencing in the nucleus (Figure 6). However, at
265 the developmental genes harboring enhancers both CSR-1 and WAGO
266 pathways appear to antagonize ectopic H3K9me deposition (Figure 6).

267 The increased intergenic enhancer RNA expression in *csr-1(tm892)* and
268 *drh-3(ne4253)* worms is likely due to indirect effects, as no secondary siRNAs
269 matching enhancers had been detected. However, we cannot exclude the
270 possibility that some non-abundant secondary siRNAs may limit enhancer RNA
271 expression, therefore antagonizing the production of long dsRNA and
272 heterochromatin formation at these regulatory regions.

273

274

275

276

DISCUSSION

The nematodes are unique in their extensive network of the *de novo* RdRP-produced small RNAs (22G RNAs). Two Argonaute proteins belonging to the WAGO group, NRDE-3 and HRDE-1, were associated with nuclear silencing processes in multiple studies, mostly involving exogenous dsRNA triggers or reporter transgenes (Guang et al., 2008; Guang et al., 2010; Burkhart et al., 2011; Burton et al., 2011; Ashe et al., 2012; Buckley et al., 2012; Gu, S.G., et al. 2012; Luteijn et al., 2012; Shirayama et al., 2012). Nuclear RNAi in *C. elegans* has been largely associated with secondary small RNAs generated in the cytoplasm and moving to the nucleus to execute their function. They are considered to be functionally equivalent to the nuclear dsRNA-derived Dicer products in fission yeast, a mechanistically well-studied system of RNAi-induced transcriptional silencing and heterochromatin formation (Cecere and Grishok, 2014). However, other reports, most notably those describing a competition between ADARs and the antiviral RNAi pathway components for nuclear dsRNA, strongly suggest that another Dicer-dependent RNAi process must initiate in the nucleus (Warf et al., 2012; Reich et al., 2018). Indeed, a recent publication characterized ectopic RNAi silencing taking place in the *adar-1/2* mutant worms (Reich et al., 2018), although this silencing had not yet been connected to chromatin changes.

Here, we uncovered a surprising role of the *C. elegans* secondary siRNA system in inhibiting dsRNA production in the nucleus and ectopic heterochromatin deposition associated with this. We propose that siRNAs

produced by the Dicer cleavage guide this process. This new silencing pathway can be more readily related to organisms lacking RdRPs, such as *Drosophila* and mammals.

Our work relates the new ectopic nuclear RNAi pathway to both H3K9 and H3K27 methylation marks. Both marks were shown to be artificially induced on active genes targeted by exogenous dsRNA (Guang et al., 2010; Mao et al., 2015). However, it was not possible to reliably correlate NRDE-3 or HRDE-1 function in regulation of endogenous genes with these silencing modification marks (Gu et al., 2012). Notably, only in the *drh-3(ne4253)* mutant background, when both CSR-1 and WAGO pathways are inactive, dramatic chromatin rearrangements take place. Our results suggest that, in *drh-3(ne4253),* a loss of CSR-1 binding to its target pre-mRNAs may allow them to hybridize with antisense RNAs, before the latter get degraded, and produce dsRNA, which becomes processed into siRNAs by Dicer. At the same time, histone methyltransferase (HMT) complexes normally working with WAGO may become available and get distributed into the freed “CSR-1 territory”. Thus, the new siRNAs and HMTs could now co-operate in inducing chromatin changes. The ectopic deposition of H3K27me3 at CSR-1 targets in *drh-3(ne4253)* may occur through such a mechanism.

At the tissue-specific spermatogenesis genes, a loss of H3K27me3 takes place in *drh-3(ne4253).* This is accompanied by ectopic expression of these genes in *drh-3(ne4253)* L2 larvae (Supplementary figure 4). However, we have not observed this increased expression in neither *nrde-3(gg64)* nor *hrde-*

323 *1(tm1200)* mutant worms (Supplementary figure 4). Both NRDE-3 and HRDE-1,
324 in the complexes with 22G RNAs, strongly interact with their target pre-mRNAs
325 (Guang et al., 2008; Ashe et al., 2012; Buckley et al., 2012; Shirayama et al.,
326 2012). It is possible that when NRDE-3 or HRDE-1 are missing, their target pre-
327 mRNAs may also engage with antisense RNAs and form dsRNA. In this case,
328 the dsRNA-induced silencing will substitute for the silencing role of WAGOs. The
329 absence of both CSR-1-bound siRNAs and WAGO-bound siRNAs may create
330 further competition for HMTs and lead to reduction of H3K27me3 at the tissue-
331 specific genes.

332 Interestingly, in the case of H3K9me3 re-distribution, both CSR-1 and
333 WAGO appear to cooperate in preventing dsRNA formation and deposition of
334 this silencing mark at the enhancer elements. We have also detected a
335 competition between the CSR-1 and WAGO pathways: CSR-1 appears to protect
336 its targets from the deposition of H3K9me3, likely guided by WAGO. This result is
337 consistent with the published work (Seth et al., 2013; Wedeles et al., 2013; Shen
338 et al., 2018).

339 Notably, the re-distribution of H3K27me3 to active autosomal genes (i.e.
340 CSR-1 targets) also occurs in the absence of H3K36 methylation at these genes
341 in the germlines of *mes-4* mutant worms (Gaydos et al., 2012). The H3K36
342 methyltransferase in yeast has been implicated in suppressing antisense
343 transcription (Venkatesh et al., 2016), and it is possible that in *C. elegans* and
344 other animals it prevents dsRNA formation and ectopic silencing of active genes.
345 Importantly, an independent line of research from our lab identified a role for

346 H3K79 methylation in suppressing dsRNA formation and RNAi-induced
347 H3K9me2 deposition at the enhancers (manuscript under consideration).
348 Therefore, research in *C. elegans* identified multiple mechanisms that have
349 evolved to suppress the inappropriate nuclear RNAi. Some of them, such as
350 ADAR action (Warf et al., 2012), H3K79 methylation, and possibly H3K36
351 methylation, are likely to be conserved.

352 Another mechanism shown to inhibit antisense RNA accumulation in
353 organisms ranging from plants to mammals is the nuclear exosome-driven
354 antisense transcript degradation (Pefanis et al., 2014; Pefanis et al., 2015). It
355 was first shown to inhibit nuclear small RNA production in plants (Chekanova et
356 al., 2007), and possibly plays a similar role across species. Finally, although the
357 nuclear dsRNA inhibition via the secondary siRNA system that we describe here
358 is unique to nematodes, other protein complexes interacting with pre-mRNAs,
359 such as splicing factors, may have this additional role.
360
361
362
363
364
365
366
367
368

MATERIALS AND METHODS

Strains

Strains were maintained at 20 °C unless otherwise noted, using standard methods (Brenner, 1974). Bristol N2 was the WT strain used. Strains used in this study were *drh-3(ne4253)* and *csr-1(tm892).* For the ChIP-seq experiments, worm populations were synchronized and grown for approximately 40 h after hatching at 20 °C on OP-50 *E. coli* at a density of ~50,000 animals per 15-cm Petri dish until they reached L3 stage. For steady-state expression analysis, worm populations were grown 5-7 h after synchronization.

ChIP

Chromatin immunoprecipitation was performed following the modENCODE Protocol from the Lieb Lab (modENCODE Consortium et al., 2009) with some modifications. The worm pellet fixed with 2% PFA for 30 minutes at 20°C was washed in M9 3 times and resuspended in RIPA buffer supplemented with Protease inhibitors (Thermo Scientific, 78443). DNA fragmentation was performed using sonication on Covaris (Peak power 240, Duty factor 20, Cycles/burst 200, 8 min). Then, 1.5–2mg of cross-linked chromatin extract was incubated at 4°C ON with a specific antibody and the immune complexes were then incubated with 50 µl IgG Dynabeads (Invitrogen) for 3h at 4°C. DNA was cleaned up with the Qiagen PCR purification kit. We used the following

antibodies: 5 µg of anti-H3K27me3 (Diagenode, pAb-195-050), 5 µg of anti-H3K36me3 (Abcam, ab9050), 5 µg of anti-H3K9me3 (Abcam, ab8898). Validation information for the commercial antibodies is included at the manufacturers' websites.

Library preparation, sequencing and data processing

ChIP-seq libraries were prepared using TruSeq Illumina kit (set A – 15034288, set B - 15034289) according to manufacturer's instructions. The sequencing was performed on Illumina NextSeq 500 Next-Generation Sequencing equipment. The 75-bp single-end Illumina sequencing reads were preprocessed by trimming the adapter sequences with Cutadapt (Didion et al., 2017). After that, reads were aligned to the WS220/ce10 assembly of the *C. elegans* genome using Bowtie for Illumina (Galaxy Version 1.1.2) (Langmead et al., 2009) with default settings. The SAMtools (Galaxy Version 1.1.2) (Li et al., 2009; Li, 2011) utility was used to convert the alignments to BAM format. The table containing the number of reads aligned to genome is included in supplementary data (Table 1).

Two independent ChIP experiments were performed with each type of antibody. Comparison of the results demonstrated the good reproducibility of the data (Supplementary table 2). Duplicates reads were removed, and the data was processed as described below.

Analysis of GRO-Seq Data

GRO-seq reads (Cecere et al., 2014) were aligned to the WS220/ce10 assembly of the C. elegans genome using Bowtie for Illumina (Galaxy Version 1.1.2) (Langmead et al., 2009) with default settings. Reads matching ribosomal RNA

loci were removed, as described before (Cecere et al., 2013). Read counting in regions (either genes, regions or genomic bins) was performed with package GenomicAlignments (Lawrence et al., 2013); only reads with mapping quality 20 or higher were included in subsequent analyses. Regions without reads across the sample set were removed. Counts were then normalized using the TMM method, which takes RNA composition bias into account (Robinson and Oshlack, 2010), using the edgeR package(Robinson et al., 2010). Coverage was expressed as RPKM (reads per kilobase per million mapped) and log2-transformed.

Analysis of ChIP-seq Data

Analysis of ChIP-seq data was performed as described for the analysis of GRO-seq data, with the exception that, after normalization of read counts, coverage was expressed as the log2-transformed ratio of the RPKM value in the immunoprecipitated DNA sample divided by the RPKM value in the non-immunoprecipitated (input) DNA. Only regions in which the normalized count value in the immunoprecipitated DNA sample was higher than that in the corresponding input DNA in at least one sample in the set were considered.

Analysis of Chromatin Domains and ATAC-seq Peaks

Coordinates of chromatin domains were obtained from Evans et al., 2016.

Putative enhancer regions were obtained by combining coordinates of domains 8, 9 and 10. Enhancer domains at least 1500 bp distal to any annotated transcription start site or transcription termination site were considered distal enhancer domains. Enhancer domains intersecting coordinates of genes < 15kb

by at least 50 bp were considered intragenic enhancer domains. ATAC-seq peak coordinates (Daugherty et al., 2017) were downloaded from the NCBI GEO database (GSE89608). Distal and intragenic ATAC-seq peaks were obtained as for enhancer domains. CSR-1 target genes were obtained from (Claycomb et al., 2009). Gene identifiers were converted to Refseq mRNA IDs using the WormBase Converter utility (http://wormbasemanager.sourceforge.net/) and the DAVID Gene ID Conversion Tool (Huang et al., 2008). Intersections of genomic intervals were performed in R using the valr package (Riemondy et al., 2017).

Small RNA bioinformatics analyses

Small RNA library sequences were downloaded from the NCBI Gene Expression Omnibus and Sequence Read Archive under the following accessions: GSM454002, GSM455389, GSM455390, GSM455387, GSM455388, SRR030720, SRR030721, SRR030722, SRR030719, and SRR030717. Fastq files were validated and adapters were trimmed with the programs Fastqc (Brown et al., 2017) and Cutadapt (Didion et al., 2017), respectively. The genome and Refseq transcript assemblies for “ce10” were loaded into our custom “gene-centric process” small RNA analyses pipeline (Sytnikova et al., 2014; Chirn et al., 2015). This program maps small RNAs with Bowtie1 (Langmead et al., 2009) with a maximum of 2 base mismatches, counts the genomic strand reads against the Ensembl gene transcript models using Bedtools (Quinlan, 2014) using the longest transcript isoform as the main gene model, and generates WIG plots for coverage visualization on the UCSC Genome Browser (Speir et al., 2016). Each

library's read counts were normalized against library depths (counts per million, cpm), as well as frequency of genomic locations (cpm / number of genomic loci).

Immunostaining

Young adult worms were handpicked and placed in M9 solution supplemented with 0.01% Tween and 25mM sodium azide on a slide. Worms were dissected using scalpel and fixed with 2% PFA for one hour at room temperature and post-fixed in ice-cold methanol for 5 minutes. Control worms were treated with RNase A prior to fixation at 37°C for 30 minutes to confirm the antibody specificity and then washed 3 times with M9. After fixation, worms were transferred to glass tubes and blocked with 1% BSA in M9 supplemented with 0.05% Tween-20. Blocked samples were then incubated with the J2 antibody (1:1000) overnight at 4°C, washed 3 times in washing buffer (BSA 0.25%, Tween-20 0.05% in M9), and then incubated with secondary fluorophore-conjugated (AF 568) antibody (1:500) for two hours in the dark room. After 3 washes, the samples were transferred to a slide and mounted with DAPI-containing solution (Invitrogen, Prolong Diamond Antifade Mountant with DAPI). The images were taken at 63x on a Zeiss AxioImager Z1 instrument and processed with ImageJ (version 1.51k).

483

484

485

486

487

488

489 FIGURE LEGENDS

490 **Figure 1. Ectopic H3K27me3 accumulation at highly expressed genes in**
491 **absence of DRH-3.** a) Open chromatin is associated with H3K36me3 histone
492 modification (pink), which opposes heterochromatin histone mark H3K27me3
493 (blue). Highly expressed genes (CSR-1 targets: *ncl-1*, *lin-13*, *snu-23*) are
494 enriched for H3K36me3 and depleted of H3K27me3. H3K27me3 is abundant at
495 low expressed/silent regions. The peaks were generated with MACS2 peak
496 calling algorithm (Galaxy version 2.0.10.2) (Zhang et al., 2008). b) ChIP-seq
497 normalized coverage for H3K36me3 (pink) and H3K27me3 (blue) demonstrating
498 the decrease of H3K36me3 in *drh-3(ne4253)* mutant compared to wild type and
499 increase in H3K27me3 modification in highly expressed CSR-1 target gene *bet-*
500 *2*. c) Global increase in H3K27me3 and reduction of H3K36me3 on highly
501 expressed CSR-1 target genes in *drh-3(ne4253)* mutant, but not in *csr-1(tm892)*
502 mutant. The normalization of both replicated was performed as described in
503 Materials and Methods. The genome was divided into 50 bp bins and $\log_2$ fold
504 change of bin coverage ratio between mutant strain and wild type was calculated.
505 Only the subclass of highly active genes (CSR-1 targets) is represented. The

colors reflect the histone mark enrichment (red) and depletion (blue) observed in both biological replicates. d) Heatmap demonstrating an increase in heterochromatic modification H3K27me3 and the decrease in activating modification H3K36me3 in actively transcribed gene coding regions in *drh-3(ne4253)* mutant compared to wild type. The genome was divided into 50 bp bins and the ratio of normalized bin coverage between mutant and wild type was plotted on a heatmap. Each row corresponds to a CSR-1 target gene body between transcription start site (TSS) and transcription termination site (TTS) +/- 200 bp. Different gene length was approximated to be 1000 bp for the representation purpose. The mean value of 2 biological replicates was plotted.

Figure 2. H3K9me3 alterations at actively transcribed genes and enhancers in *csr-1(tm892)* and *drh-3(ne4253)*. a) H3K9me3 distribution along the chromosomes demonstrates that, on *C. elegans* autosomes, H3K9me3 is enriched at the chromosome arms and, on the X chromosome, only at the left arm. Read coverage in wild type worms (L3) normalized to, consequently, RPKM and input is represented. b) Box plot demonstrating increase of H3K9 methylation in CSR-1 target genes in *csr-1(tm892)*, but not in *drh-3(ne4253)*. ChIP-seq data were normalized as described in methods. *P-value<$2.2*10^{-16}$(Wilcoxon test) c) Box plots and cumulative plots demonstrating H3K9me3 increase at enhancers detected by ATAC-Seq (Daugherty et al., 2017) in *csr-1(tm892)* and *drh-3(ne4253)* mutants compared to wild type.

Figure 3. Bidirectional transcription is increased at enhancer regions in *csr-1(tm892)* and *drh-3(ne4253)*.

a) Box plot representing increase of sense GRO-Seq read coverage (Cecere et al., 2014) at enhancer-containing transcripts in L3 larva *csr-1(tm892)* mutant. Gro-Seq data (Cecere et al., 2014) was normalized as described in methods and $\log_2$ transformed RPKM was plotted. *P-values <0.01 b) Same for *drh-3(ne4253)* mutant. c) Box plot representing increase of antisense GRO-Seq read coverage (Cecere et al., 2014) at enhancer-containing transcripts and CSR-1 targets containing enhancers in L3 larva *csr-1(tm892)* mutant. *P-values <0.01 d) Same for *drh-3(ne4253)* mutant.

Figure 4. Elevated transcription at enhancer regions in *csr-1(tm892)* and *drh-3(ne4253)*. a) Box plot demonstrating increase of total GRO-seq read coverage at putative enhancers (Evans et al., 2016) in *csr-1(tm892)* L3 larva (left) and in *drh-3 (ne4253)* (right). GRO-seq data (Cecere et al., 2014) were normalized as described in methods and $\log_2$ transformed RPKM was plotted. *P-values $<2.2*10^{-16}$. b) GRO-seq read coverage is increased at enhancer regions in *csr-1(tm892)* (left panel) and *drh-3(ne4253)* (right panel). The increase is more pronounced at distal enhancers than at intragenic enhancers (ATAC-seq peaks). *P-values <0.01. Analysis was performed as in (a). Cumulative plots confirming the GRO-seq data analysis for *csr-1(tm892)* (on the left) and *drh-3(ne4253)* (on the right) and demonstrating an increase of GRO-seq reads coverage in both mutants. The latter is especially clear at intergenic (distal) enhancers (ATAC-seq

552 data by (Daugherty et al., 2017)). c) GRO-seq reads corresponding to antisense
553 transcription are shown at the region containing an enhancer detected by ATAC-
554 seq upstream of the *daf-12* gene. The increase in the number of antisense reads
555 is shown in *drh-3(ne4253)* (blue) and *csr-1(tm892)* (green) compared to wild type
556 (grey).
557
558 **Figure 5. A shift to equally abundant sense and antisense small RNAs in**
559 **the RdRP-mutants and *csr-1(tm892)*.**
560 a) A decreased ratio of antisense/total small RNAs in RdRP mutants and *csr-*
561 *1(tm892)*. The small RNA data (Claycomb et al., 2009; Gu et al., 2009) were
562 analyzed as described in Materials and Methods. The reads corresponding to
563 miRNA and structure RNA were removed. Error bars represent 95% confidence
564 interval. b) Sense small RNAs and antisense small RNAs (depending on the
565 directionality of gene transcription) become equally abundant in RdRP mutants
566 and *csr-1(tm892)*. The region on chromosome II containing a cluster of histone
567 genes is shown. The reads on the positive strand are labeled with red and on
568 those on the negative strand are labeled with blue. The bottom track represents
569 the reads obtained by sequencing CSR-1-associated small RNAs that are
570 antisense to the direction of gene transcription. The directionality of histone
571 genes is marked with the arrows. The enlarged region demonstrates the increase
572 in both sense and antisense small RNA occupancy. c) Images demonstrating an
573 increase in nuclear dsRNA in *drh-3(ne4253)*. The worm intestines were
574 extracted, fixed and stained with J2 antibody. J2 foci preferentially accumulate in

575 the intestine nuclei. Control worms were treated with RNase A to confirm the
576 specificity of J2 antibody (Supplementary figure 3).
577
578
579
580 **Figure 6. Model demonstrating the proposed role of secondary (RdRP-**
581 **produced) small RNAs in preventing dsRNA formation and deposition of**
582 **the silencing marks at enhancer elements and active genes in *C. elegans***
583
584 SUPPLEMENTARY FIGURES
585 **Supplementary figure 1. Loss of H3K27me3 in pseudogenes and tissue-**
586 **specific genes (spermatogenesis) genes in absence of DRH-3.** a) Heatmap
587 demonstrating a decrease in heterochromatic modification H3K27me3 and the
588 increase in activating modification H3K36me3 in pseudogenes in *drh-3(ne4253)*
589 mutant compared to wild type. The genome was divided into 50 bp bins and the
590 ratio of normalized bin coverage between mutant and wild type was plotted on a
591 heatmap. Each row corresponds to pseudogene coding regions between
592 transcription start site (TSS) and transcription termination site (TTS) +/- 200 bp.
593 Different gene length was approximated to be 1000 bp for the representation
594 purpose. The mean value of 2 biological replicates is shown. b) same as on a) for
595 tissue-specific genes represented by spermatogenesis genes.
596

Supplementary figure 2. H3K9me3 levels at CSR-1 target genes in *drh-3(ne4253)*.

a) Pie chart representing the percentage of CSR-1 target genes containing enhancers**.** b) Box plots demonstrating a general decrease of H3K9me3 at CSR-1 target genes in *drh-3(ne4253)* mutant compared to wild type, with the exception of genes with the enhancers. *P-value<$2.2*10^{-16}$, **P-value=0.35, ***P-value=$3.241*10^{-15}$.

Supplementary figure 3. Images demonstrating the absence of J2 foci after treatment with RNAse A.

Supplementary figure 4. Expression of spermatogenesis genes is increased in drh-3, but not in RdRP-mutants. Expression of spermatogenesis genes was detected by real-time PCR following reverse transcription. The obtained qPCR efficiency was normalized on house-keeping gene expression *csq-1*. Two spermatogenesis genes demonstrate ectopic transcription in drh-3(ne4253) mutant, but not in RdRP-mutants. Primers: C15H7.3 (forward GAATGGTCCGGAGAGTTTCA, reverse AGCTATGCTCTCCTGGTGGA); F19B6.4 (forward AACCCTCACAGTCCGAGAGA, reverse GTCATGGTTCCGACTTTCGT); *csq-1*(forward GGCATCTCCAAAAACGAAGA, reverse ACCGATTTGGTGTCTTCAGC).

AUTHOR CONTRIBUTIONS

E.G. conducted experiments and analyzed data, R.E. analyzed data, Q.M. and N.L. analyzed small RNA data, A.G. supervised the project. E.G. and A.G. wrote the manuscript.

ACKNOWLEDGEMENTS

We are grateful to the Mello and Kennedy labs for providing RNAi mutant strains. Some strains used in this study were obtained from the *Caenorhabditis Genetics Center*, which is funded by NIH Office of Research Infrastructure Programs (P40 OD010440). We thank Dr. Cifuentes' lab for fruitful discussions and Dr. Ritter for advising us on microscopy techniques. We thankful to Yunfan (Frank) Liang for help with qPCR and immunostaining experiments.

This research was supported by the NIH R01 GM107056 award to AG.

REFERENCES

Ashe, A., Sapetschnig, A., Weick, E.-M., Mitchell, J., Bagijn, M.P., Cording, A.C., Doebley, A.-L., Goldstein, L.D., Lehrbach, N.J., Le Pen, J., et al. (2012). piRNAs Can Trigger a Multigenerational Epigenetic Memory in the Germline of C. elegans. Cell *150*, 88–99.

Brenner, S. (1974). The genetics of Caenorhabditis elegans. Genetics *77*, 71–94.

Brown, J., Pirrung, M., and McCue, L.A. (2017). FQC Dashboard: integrates FastQC results into a web-based, interactive, and extensible FASTQ quality control tool. Bioinforma. Oxf. Engl.

Buckley, B.A., Burkhart, K.B., Gu, S.G., Spracklin, G., Kershner, A., Fritz, H., Kimble, J., Fire, A., and Kennedy, S. (2012). A nuclear Argonaute promotes multigenerational epigenetic inheritance and germline immortality. Nature *489*, 447–451.

Burkhart, K.B., Guang, S., Buckley, B.A., Wong, L., Bochner, A.F., and Kennedy, S. (2011). A Pre-mRNA–Associating Factor Links Endogenous siRNAs to Chromatin Regulation. PLoS Genet. *7*, e1002249.

Burton, N.O., Burkhart, K.B., and Kennedy, S. (2011). Nuclear RNAi maintains heritable gene silencing in Caenorhabditis elegans. Proc. Natl. Acad. Sci. *108*, 19683–19688.

Cecere, G., and Grishok, A. (2014). A nuclear perspective on RNAi pathways in metazoans. Biochim. Biophys. Acta BBA - Gene Regul. Mech. *1839*, 223–233.

Cecere, G., Hoersch, S., Jensen, M.B., Dixit, S., and Grishok, A. (2013). The ZFP-1(AF10)/DOT-1 Complex Opposes H2B Ubiquitination to Reduce Pol II Transcription. Mol. Cell *50*, 894–907.

Cecere, G., Hoersch, S., O'Keeffe, S., Sachidanandam, R., and Grishok, A. (2014). Global effects of the CSR-1 RNA interference pathway on the transcriptional landscape. Nat. Struct. Mol. Biol. *21*, 358–365.

Chekanova, J.A., Gregory, B.D., Reverdatto, S.V., Chen, H., Kumar, R., Hooker, T., Yazaki, J., Li, P., Skiba, N., Peng, Q., et al. (2007). Genome-Wide High-Resolution Mapping of Exosome Substrates Reveals Hidden Features in the Arabidopsis Transcriptome. Cell *131*, 1340–1353.

Chirn, G.-W., Rahman, R., Sytnikova, Y.A., Matts, J.A., Zeng, M., Gerlach, D., Yu, M., Berger, B., Naramura, M., Kile, B.T., et al. (2015). Conserved piRNA Expression from a Distinct Set of piRNA Cluster Loci in Eutherian Mammals. PLoS Genet. *11*, e1005652.

Claycomb, J.M., Batista, P.J., Pang, K.M., Gu, W., Vasale, J.J., van Wolfswinkel, J.C., Chaves, D.A., Shirayama, M., Mitani, S., Ketting, R.F., et al. (2009). The Argonaute CSR-1 and its 22G-RNA cofactors are required for holocentric chromosome segregation. Cell *139*, 123–134.

Daugherty, A.C., Yeo, R.W., Buenrostro, J.D., Greenleaf, W.J., Kundaje, A., and Brunet, A. (2017a). Chromatin accessibility dynamics reveal novel functional enhancers in *C. elegans*. Genome Res. *27*, 2096–2107.

Daugherty, A.C., Yeo, R.W., Buenrostro, J.D., Greenleaf, W.J., Kundaje, A., and Brunet, A. (2017b). Chromatin accessibility dynamics reveal novel functional enhancers in C. elegans. Genome Res. *27*, 2096–2107.

Didion, J.P., Martin, M., and Collins, F.S. (2017). Atropos: specific, sensitive, and speedy trimming of sequencing reads. PeerJ *5*, e3720.

Evans, K.J., Huang, N., Stempor, P., Chesney, M.A., Down, T.A., and Ahringer, J. (2016a). Stable Caenorhabditis elegans chromatin domains separate broadly expressed and developmentally regulated genes. Proc. Natl. Acad. Sci. *113*, E7020–E7029.

Evans, K.J., Huang, N., Stempor, P., Chesney, M.A., Down, T.A., and Ahringer, J. (2016b). Stable *Caenorhabditis elegans* chromatin domains separate broadly expressed and developmentally regulated genes. Proc. Natl. Acad. Sci. *113*, E7020–E7029.

Gaydos, L.J., Rechtsteiner, A., Egelhofer, T.A., Carroll, C.R., and Strome, S. (2012). Antagonism between MES-4 and Polycomb Repressive Complex 2 Promotes Appropriate Gene Expression in C. elegans Germ Cells. Cell Rep. *2*, 1169–1177.

686 Gaydos, L.J., Wang, W., and Strome, S. (2014). H3K27me and PRC2 transmit a
687 memory of repression across generations and during development. Science *345*, 1515–
688 1518.

689 Grishok, A. (2005). Transcriptional silencing of a transgene by RNAi in the soma of C.
690 elegans. Genes Dev. *19*, 683–696.

691 Gu, S.G., Pak, J., Guang, S., Maniar, J.M., Kennedy, S., and Fire, A. (2012a).
692 Amplification of siRNA in Caenorhabditis elegans generates a transgenerational
693 sequence-targeted histone H3 lysine 9 methylation footprint. Nat. Genet. *44*, 157–164.

694 Gu, S.G., Pak, J., Guang, S., Maniar, J.M., Kennedy, S., and Fire, A. (2012b).
695 Amplification of siRNA in Caenorhabditis elegans generates a transgenerational
696 sequence-targeted histone H3 lysine 9 methylation footprint. Nat. Genet. *44*, 157–164.

697 Gu, W., Shirayama, M., Conte, D., Vasale, J., Batista, P.J., Claycomb, J.M., Moresco,
698 J.J., Youngman, E.M., Keys, J., Stoltz, M.J., et al. (2009). Distinct Argonaute-Mediated
699 22G-RNA Pathways Direct Genome Surveillance in the C. elegans Germline. Mol. Cell
700 *36*, 231–244.

701 Guang, S., Bochner, A.F., Pavelec, D.M., Burkhart, K.B., Harding, S., Lachowiec, J., and
702 Kennedy, S. (2008). An Argonaute transports siRNAs from the cytoplasm to the nucleus.
703 Science *321*, 537–541.

704 Guang, S., Bochner, A.F., Burkhart, K.B., Burton, N., Pavelec, D.M., and Kennedy, S.
705 (2010). Small regulatory RNAs inhibit RNA polymerase II during the elongation phase of
706 transcription. Nature *465*, 1097–1101.

707 Gullerova, M., and Proudfoot, N.J. (2012). Convergent transcription induces
708 transcriptional gene silencing in fission yeast and mammalian cells. Nat. Struct. Mol.
709 Biol. *19*, 1193–1201.

710 Han, T., Manoharan, A.P., Harkins, T.T., Bouffard, P., Fitzpatrick, C., Chu, D.S., Thierry-
711 Mieg, D., Thierry-Mieg, J., and Kim, J.K. (2009). 26G endo-siRNAs regulate
712 spermatogenic and zygotic gene expression in Caenorhabditis elegans. Proc. Natl.
713 Acad. Sci. *106*, 18674–18679.

714 Huang, D.W., Sherman, B.T., Stephens, R., Baseler, M.W., Lane, H.C., and Lempicki,
715 R.A. (2008). DAVID gene ID conversion tool. Bioinformation *2*, 428–430.

716 Langmead, B., Trapnell, C., Pop, M., and Salzberg, S.L. (2009). Ultrafast and memory-
717 efficient alignment of short DNA sequences to the human genome. Genome Biol. *10*,
718 R25.

719 Lawrence, M., Huber, W., Pagès, H., Aboyoun, P., Carlson, M., Gentleman, R., Morgan,
720 M.T., and Carey, V.J. (2013). Software for Computing and Annotating Genomic Ranges.
721 PLoS Comput. Biol. *9*, e1003118.

722 Lee, H.-C., Gu, W., Shirayama, M., Youngman, E., Conte, D., and Mello, C.C. (2012). C.
723 elegans piRNAs Mediate the Genome-wide Surveillance of Germline Transcripts. Cell
724 *150*, 78–87.

725 Li, H. (2011). A statistical framework for SNP calling, mutation discovery, association
726 mapping and population genetical parameter estimation from sequencing data.
727 Bioinforma. Oxf. Engl. *27*, 2987–2993.

728 Li, H., Handsaker, B., Wysoker, A., Fennell, T., Ruan, J., Homer, N., Marth, G.,
729 Abecasis, G., Durbin, R., and 1000 Genome Project Data Processing Subgroup (2009).
730 The Sequence Alignment/Map format and SAMtools. Bioinforma. Oxf. Engl. *25*, 2078–
731 2079.

732 Li, W., Notani, D., and Rosenfeld, M.G. (2016). Enhancers as non-coding RNA
733 transcription units: recent insights and future perspectives. Nat. Rev. Genet. *17*, 207–
734 223.

735 Liu, T., Rechtsteiner, A., Egelhofer, T.A., Vielle, A., Latorre, I., Cheung, M.-S., Ercan, S.,
736 Ikegami, K., Jensen, M., Kolasinska-Zwierz, P., et al. (2011). Broad chromosomal
737 domains of histone modification patterns in C. elegans. Genome Res. *21*, 227–236.

738 Luteijn, M.J., van Bergeijk, P., Kaaij, L.J.T., Almeida, M.V., Roovers, E.F., Berezikov, E.,
739 and Ketting, R.F. (2012). Extremely stable Piwi-induced gene silencing in
740 Caenorhabditis elegans. EMBO J. *31*, 3422–3430.

741 Mao, H., Zhu, C., Zong, D., Weng, C., Yang, X., Huang, H., Liu, D., Feng, X., and
742 Guang, S. (2015). The Nrde Pathway Mediates Small-RNA-Directed Histone H3 Lysine
743 27 Trimethylation in Caenorhabditis elegans. Curr. Biol. *25*, 2398–2403.

744 Moazed, D., Buhler, M., Buker, S.M., Colmenares, S.U., Gerace, E.L., Gerber, S.A.,
745 Hong, E.-J.E., Motamedi, M.R., Verdel, A., Villen, J., et al. (2006). Studies on the
746 Mechanism of RNAi-dependent Heterochromatin Assembly. Cold Spring Harb. Symp.
747 Quant. Biol. *71*, 461–471.

748 modENCODE Consortium, Celniker, S.E., Dillon, L.A.L., Gerstein, M.B., Gunsalus, K.C.,
749 Henikoff, S., Karpen, G.H., Kellis, M., Lai, E.C., Lieb, J.D., et al. (2009). Unlocking the
750 secrets of the genome. Nature *459*, 927–930.

751 Ni, J., Chen, E., and Gu, S. (2014). Complex coding of endogenous siRNA,
752 transcriptional silencing and H3K9 methylation on native targets of germline nuclear
753 RNAi in C. elegans. BMC Genomics *15*, 1157.

754 Pefanis, E., Wang, J., Rothschild, G., Lim, J., Chao, J., Rabadan, R., Economides, A.N.,
755 and Basu, U. (2014). Noncoding RNA transcription targets AID to divergently transcribed
756 loci in B cells. Nature *514*, 389–393.

757 Pefanis, E., Wang, J., Rothschild, G., Lim, J., Kazadi, D., Sun, J., Federation, A., Chao,
758 J., Elliott, O., Liu, Z.-P., et al. (2015). RNA Exosome-Regulated Long Non-Coding RNA
759 Transcription Controls Super-Enhancer Activity. Cell *161*, 774–789.

760 Pikaard, C.S., and Mittelsten Scheid, O. (2014). Epigenetic Regulation in Plants. Cold
761 Spring Harb. Perspect. Biol. *6*, a019315–a019315.

762 Quinlan, A.R. (2014). BEDTools: The Swiss-Army Tool for Genome Feature Analysis.
763 Curr. Protoc. Bioinforma. *47*, 11.12.1-34.

764 Reich, D.P., Tyc, K.M., and Bass, B.L. (2018). *C. elegans* ADARs antagonize silencing
765 of cellular dsRNAs by the antiviral RNAi pathway. Genes Dev. *32*, 271–282.

766 Reinhart, B.J. (2002). Small RNAs Correspond to Centromere Heterochromatic Repeats.
767 Science *297*, 1831–1831.

768 Riemondy, K.A., Sheridan, R.M., Gillen, A., Yu, Y., Bennett, C.G., and Hesselberth, J.R.
769 (2017). valr: Reproducible genome interval analysis in R. F1000Research *6*, 1025.

770 Robinson, M.D., and Oshlack, A. (2010). A scaling normalization method for differential
771 expression analysis of RNA-seq data. Genome Biol. *11*.

772 Robinson, M.D., McCarthy, D.J., and Smyth, G.K. (2010). edgeR: a Bioconductor
773 package for differential expression analysis of digital gene expression data.
774 Bioinformatics *26*, 139–140.

775 Sarkies, P., Ashe, A., Le Pen, J., McKie, M.A., and Miska, E.A. (2013). Competition
776 between virus-derived and endogenous small RNAs regulates gene expression in
777 Caenorhabditis elegans. Genome Res. *23*, 1258–1270.

778 Schmitges, F.W., Prusty, A.B., Faty, M., Stützer, A., Lingaraju, G.M., Aiwazian, J., Sack,
779 R., Hess, D., Li, L., Zhou, S., et al. (2011). Histone Methylation by PRC2 Is Inhibited by
780 Active Chromatin Marks. Mol. Cell *42*, 330–341.

781 Seth, M., Shirayama, M., Gu, W., Ishidate, T., Conte, D., and Mello, C.C. (2013). The C.
782 elegans CSR-1 argonaute pathway counteracts epigenetic silencing to promote germline
783 gene expression. Dev. Cell *27*, 656–663.

784 Shen, E.-Z., Chen, H., Ozturk, A.R., Tu, S., Shirayama, M., Tang, W., Ding, Y.-H., Dai,
785 S.-Y., Weng, Z., and Mello, C.C. (2018). Identification of piRNA Binding Sites Reveals
786 the Argonaute Regulatory Landscape of the C. elegans Germline. Cell *172*, 937-
787 951.e18.

788 Shirayama, M., Seth, M., Lee, H.-C., Gu, W., Ishidate, T., Conte, D., and Mello, C.C.
789 (2012). piRNAs Initiate an Epigenetic Memory of Nonself RNA in the C. elegans
790 Germline. Cell *150*, 65–77.

791 Speir, M.L., Zweig, A.S., Rosenbloom, K.R., Raney, B.J., Paten, B., Nejad, P., Lee, B.T.,
792 Learned, K., Karolchik, D., Hinrichs, A.S., et al. (2016). The UCSC Genome Browser
793 database: 2016 update. Nucleic Acids Res. *44*, D717-725.

794 Sytnikova, Y.A., Rahman, R., Chirn, G.-W., Clark, J.P., and Lau, N.C. (2014).
795 Transposable element dynamics and PIWI regulation impacts lncRNA and gene
796 expression diversity in Drosophila ovarian cell cultures. Genome Res. *24*, 1977–1990.

797 Tabara, H., Yigit, E., Siomi, H., and Mello, C.C. (2002). The dsRNA binding protein RDE-
798 4 interacts with RDE-1, DCR-1, and a DExH-box helicase to direct RNAi in C. elegans.
799 Cell *109*, 861–871.

800 Tam, O.H., Aravin, A.A., Stein, P., Girard, A., Murchison, E.P., Cheloufi, S., Hodges, E.,
801 Anger, M., Sachidanandam, R., Schultz, R.M., et al. (2008). Pseudogene-derived small
802 interfering RNAs regulate gene expression in mouse oocytes. Nature *453*, 534–538.

803 Tsai, H.-Y., Chen, C.-C.G., Conte, D., Moresco, J.J., Chaves, D.A., Mitani, S., Yates,
804 J.R., Tsai, M.-D., and Mello, C.C. (2015). A Ribonuclease Coordinates siRNA
805 Amplification and mRNA Cleavage during RNAi. Cell *160*, 407–419.

806 Vasale, J.J., Gu, W., Thivierge, C., Batista, P.J., Claycomb, J.M., Youngman, E.M.,
807 Duchaine, T.F., Mello, C.C., and Conte, D. (2010). Sequential rounds of RNA-dependent
808 RNA transcription drive endogenous small-RNA biogenesis in the ERGO-1/Argonaute
809 pathway. Proc. Natl. Acad. Sci. *107*, 3582–3587.

810 Venkatesh, S., Li, H., Gogol, M.M., and Workman, J.L. (2016). Selective suppression of
811 antisense transcription by Set2-mediated H3K36 methylation. Nat. Commun. *7*, 13610.

812 Warf, M.B., Shepherd, B.A., Johnson, W.E., and Bass, B.L. (2012). Effects of ADARs on
813 small RNA processing pathways in C. elegans. Genome Res. *22*, 1488–1498.

814 Watanabe, T., Totoki, Y., Toyoda, A., Kaneda, M., Kuramochi-Miyagawa, S., Obata, Y.,
815 Chiba, H., Kohara, Y., Kono, T., Nakano, T., et al. (2008). Endogenous siRNAs from
816 naturally formed dsRNAs regulate transcripts in mouse oocytes. Nature *453*, 539–543.

817 Wedeles, C.J., Wu, M.Z., and Claycomb, J.M. (2013). Protection of germline gene
818 expression by the C. elegans Argonaute CSR-1. Dev. Cell *27*, 664–671.

819 Yigit, E., Batista, P.J., Bei, Y., Pang, K.M., Chen, C.-C.G., Tolia, N.H., Joshua-Tor, L.,
820 Mitani, S., Simard, M.J., and Mello, C.C. (2006). Analysis of the C. elegans Argonaute
821 Family Reveals that Distinct Argonautes Act Sequentially during RNAi. Cell *127*, 747–
822 757.

823 Yuan, W., Xu, M., Huang, C., Liu, N., Chen, S., and Zhu, B. (2011). H3K36 Methylation
824 Antagonizes PRC2-mediated H3K27 Methylation. J. Biol. Chem. *286*, 7983–7989.

825 Zhang, Y., Liu, T., Meyer, C.A., Eeckhoute, J., Johnson, D.S., Bernstein, B.E.,
826 Nussbaum, C., Myers, R.M., Brown, M., Li, W., et al. (2008). Model-based Analysis of
827 ChIP-Seq (MACS). Genome Biol. *9*, R137.

828

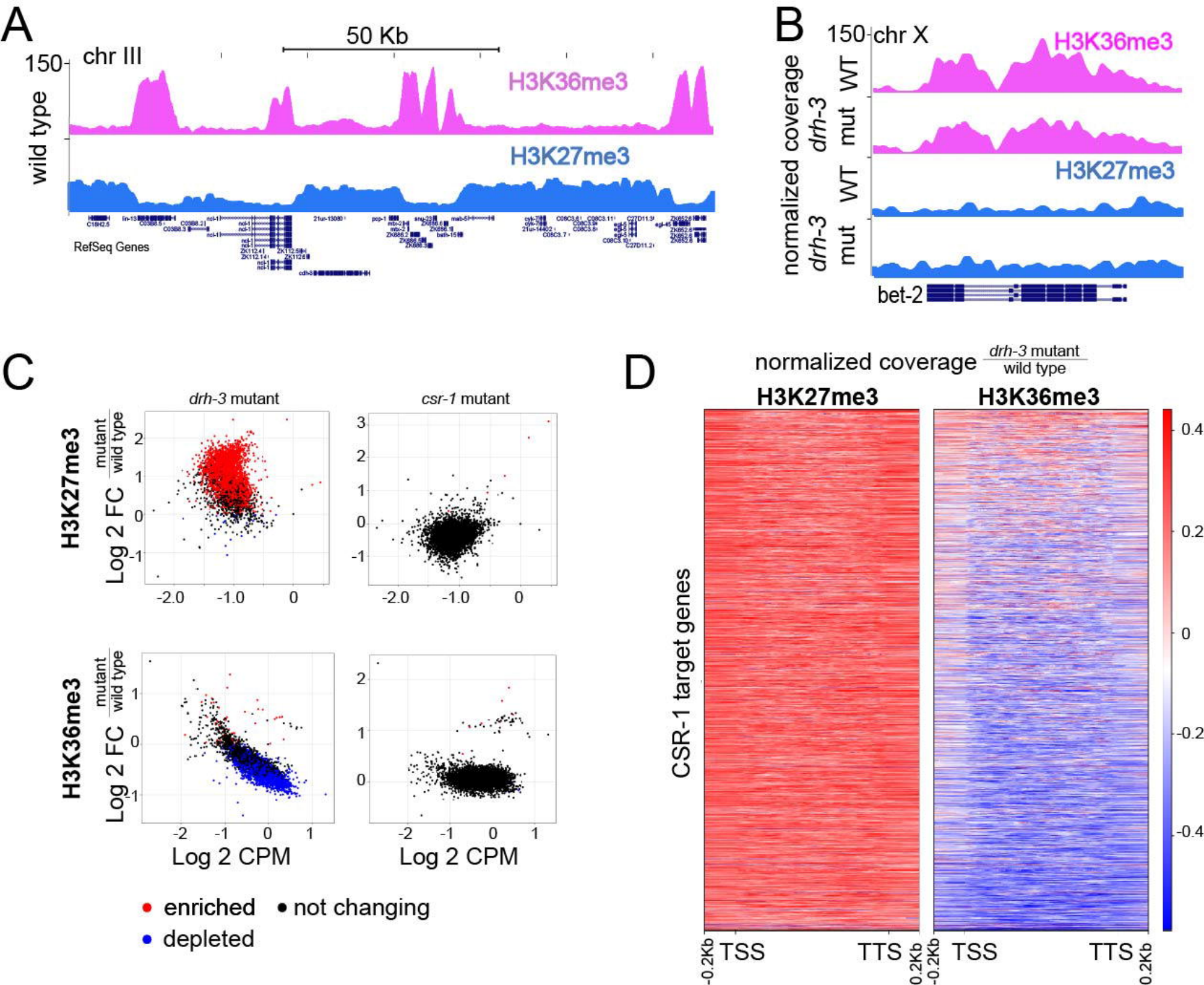
A
50 Kb
chr III
150
wild type
H3K36me3
H3K27me3
RefSeq Genes
B
150
chr X
H3K36me3
normalized coverage
drh-3
WT
mut
H3K27me3
drh-3
WT
mut
bet-2
C
drh-3 mutant
csr-1 mutant
H3K27me3
mutant / wild type
Log 2 FC
H3K36me3
mutant / wild type
Log 2 FC
Log 2 CPM
Log 2 CPM
enriched
not changing
depleted
D
normalized coverage
drh-3 mutant / wild type
H3K27me3
H3K36me3
CSR-1 target genes
-0.2Kb
TSS
TTS
0.2Kb
-0.2Kb
TSS
TTS
0.2Kb
0.4
0.2
0
-0.2
-0.4

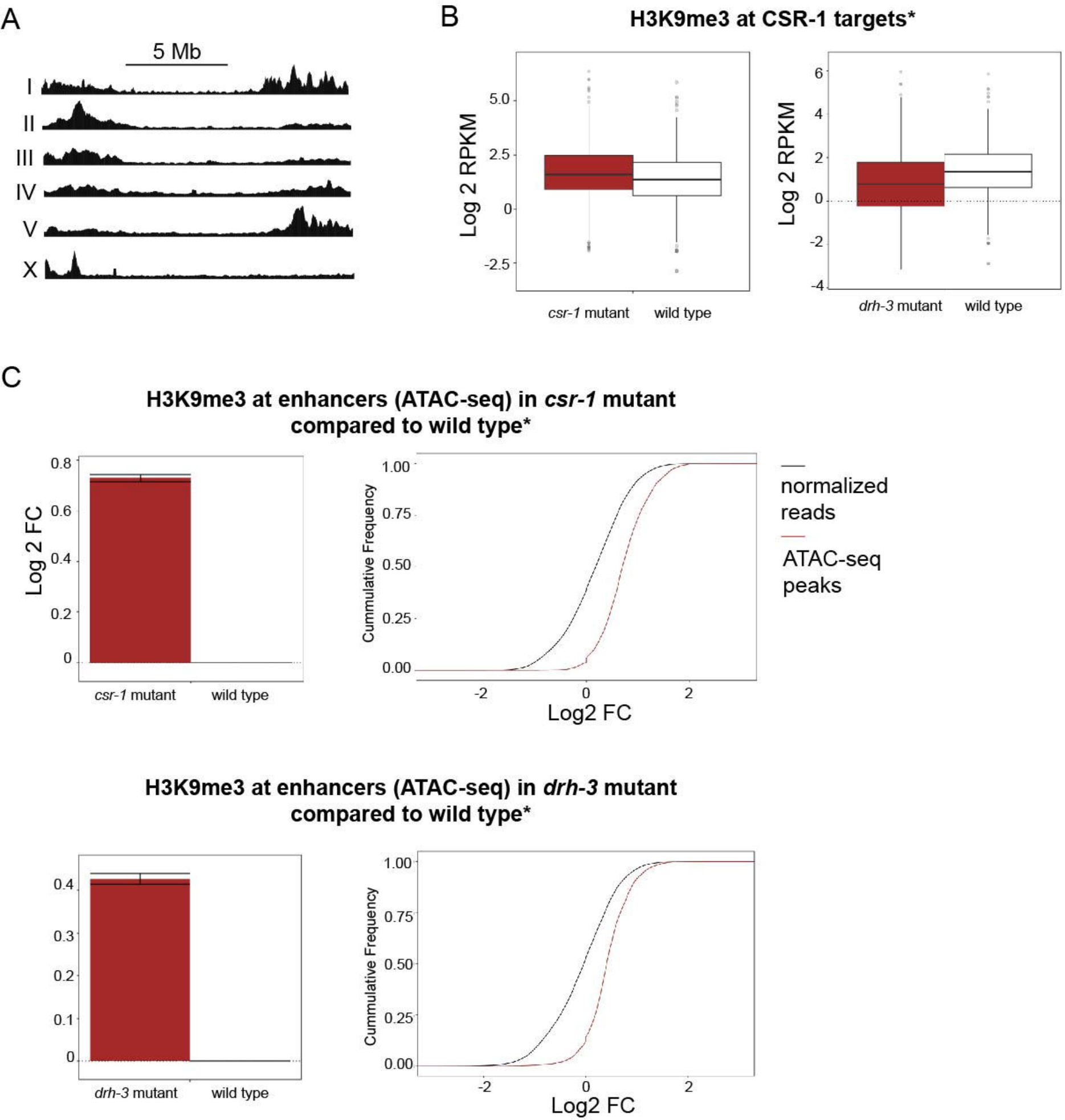
A
5 Mb
I
II
III
IV
V
X
B
H3K9me3 at CSR-1 targets*
Log 2 RPKM
5.0
2.5
0
-2.5
csr-1 mutant
wild type
Log 2 RPKM
6
4
2
0
-2
-4
drh-3 mutant
wild type
C
H3K9me3 at enhancers (ATAC-seq) in csr-1 mutant compared to wild type*
Log 2 FC
0.8
0.6
0.4
0.2
0
csr-1 mutant
wild type
Cummulative Frequency
1.00
0.75
0.50
0.25
0.00
-2
0
2
Log2 FC
normalized reads
ATAC-seq peaks
H3K9me3 at enhancers (ATAC-seq) in drh-3 mutant compared to wild type*
0.4
0.3
0.2
0.1
0
drh-3 mutant
wild type
Cummulative Frequency
1.00
0.75
0.50
0.25
0.00
-2
0
2
Log2 FC

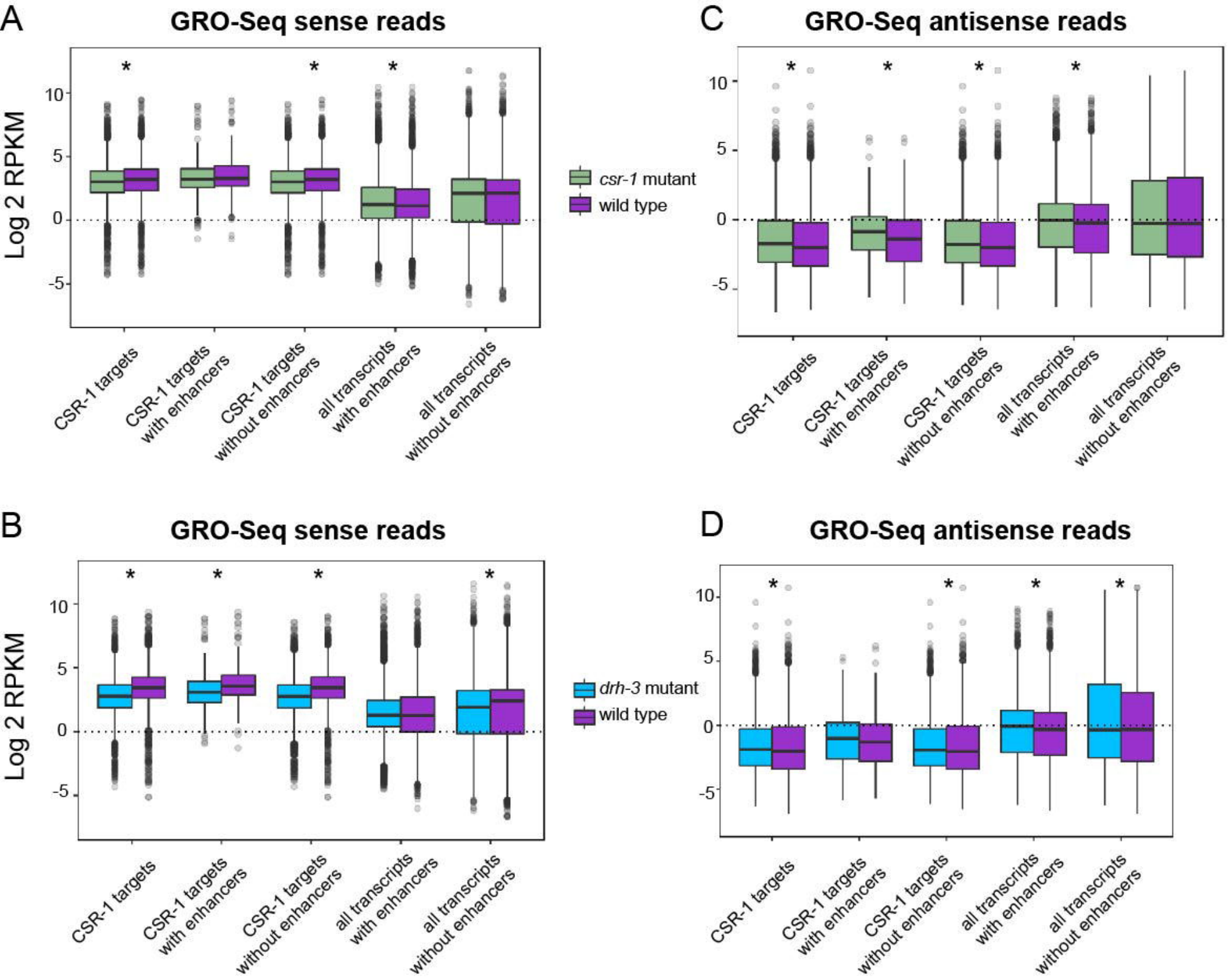
A
GRO-Seq sense reads
Log 2 RPKM
10
5
0
-5
*
*
*
CSR-1 targets
CSR-1 targets with enhancers
CSR-1 targets without enhancers
all transcripts with enhancers
all transcripts without enhancers
csr-1 mutant
wild type
C
GRO-Seq antisense reads
B
GRO-Seq sense reads
drh-3 mutant
D
GRO-Seq antisense reads

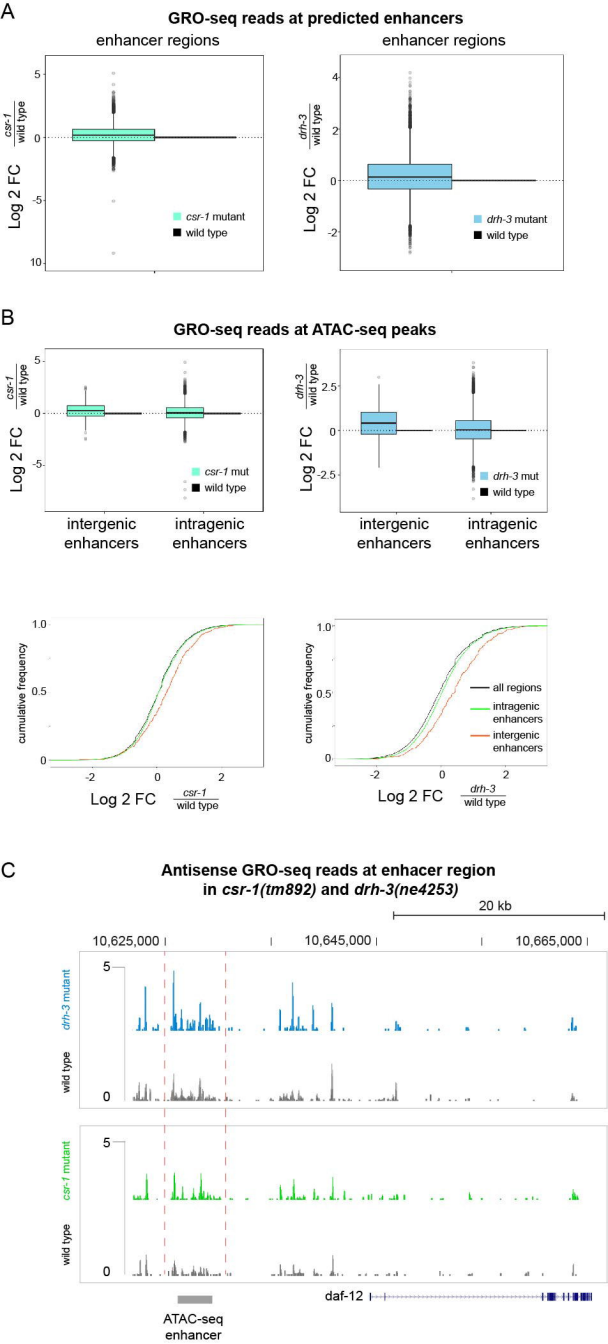
A
GRO-seq reads at predicted enhancers
enhancer regions
csr-1 / wild type
Log 2 FC
csr-1 mutant
wild type
enhancer regions
drh-3 / wild type
Log 2 FC
drh-3 mutant
wild type
B
GRO-seq reads at ATAC-seq peaks
csr-1 / wild type
Log 2 FC
csr-1 mut
wild type
intergenic enhancers
intragenic enhancers
drh-3 / wild type
Log 2 FC
drh-3 mut
wild type
intergenic enhancers
intragenic enhancers
cumulative frequency
Log 2 FC csr-1 / wild type
cumulative frequency
all regions
intragenic enhancers
intergenic enhancers
Log 2 FC drh-3 / wild type
C
Antisense GRO-seq reads at enhacer region
in csr-1(tm892) and drh-3(ne4253)
20 kb
10,625,000
10,645,000
10,665,000
drh-3 mutant
wild type
csr-1 mutant
wild type
ATAC-seq enhancer
daf-12

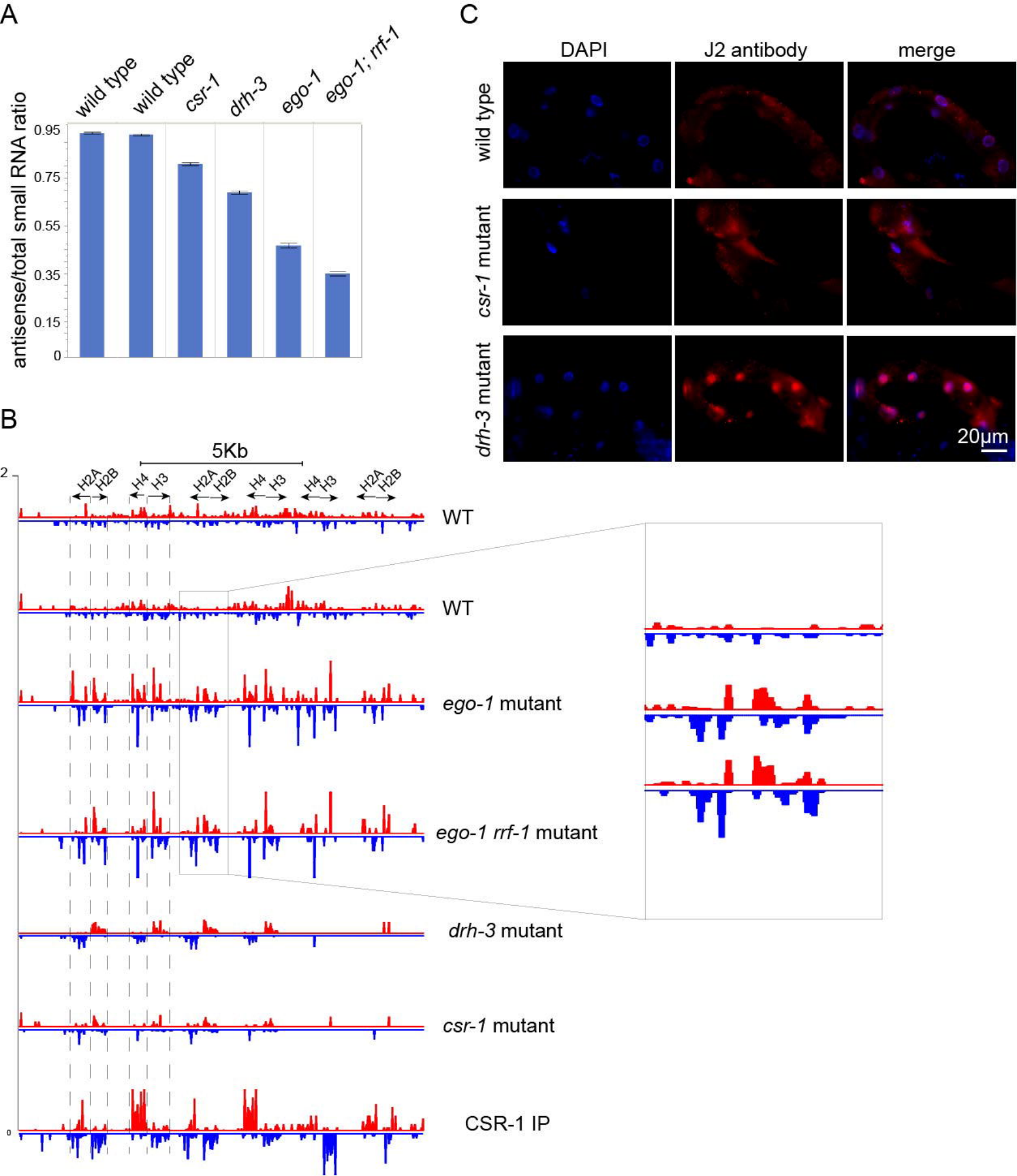
A
wild type
wild type
csr-1
drh-3
ego-1
ego-1; rrf-1
antisense/total small RNA ratio
0.95
0.75
0.55
0.35
0.15
0
C
DAPI
J2 antibody
merge
wild type
csr-1 mutant
drh-3 mutant
20μm
B
5Kb
H2A
H2B
H4
H3
WT
WT
ego-1 mutant
ego-1 rrf-1 mutant
drh-3 mutant
csr-1 mutant
CSR-1 IP

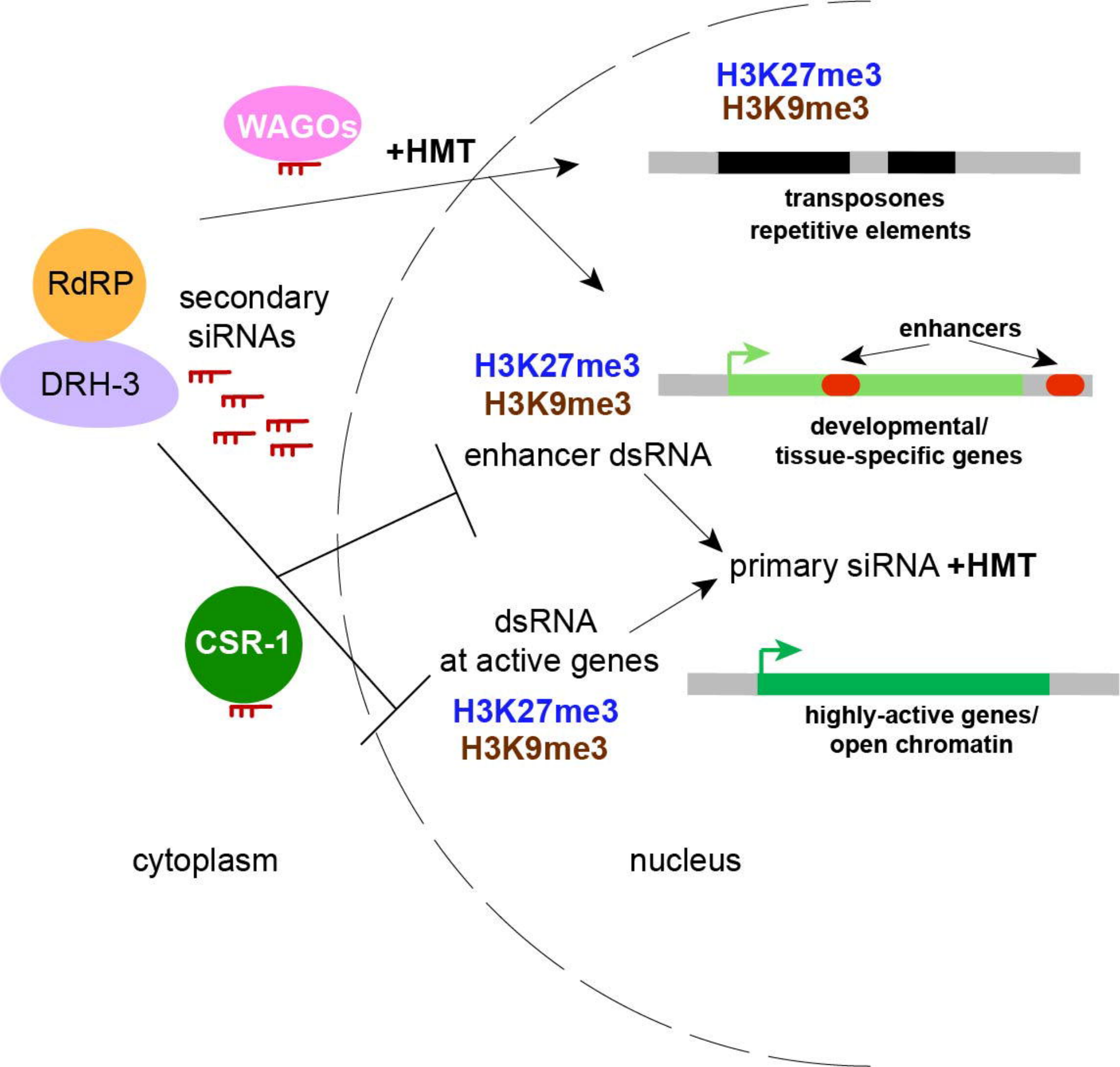
WAGOs
+HMT
H3K27me3
H3K9me3
transposones
repetitive elements
RdRP
DRH-3
secondary
siRNAs
enhancers
H3K27me3
H3K9me3
developmental/
tissue-specific genes
enhancer dsRNA
primary siRNA +HMT
CSR-1
dsRNA
at active genes
H3K27me3
H3K9me3
highly-active genes/
open chromatin
cytoplasm
nucleus